Journal of Advanced Ceramics
2020, **9**(3): 329–338
https://doi.org/10.1007/s40145-020-0372-y
ISSN 2226-4108
CN 10-1154/TQ

Research Article

Study of the structural, ferroelectric, dielectric, and pyroelectric properties of the $K_{0.5}Na_{0.5}NbO_3$ system doped with Li^+, La^{3+}, and Ti^{4+}

C. MONTERO-TAVERA[a], M. D. DURRUTHY-RODRÍGUEZ[b], F. D. CORTÉS-VEGA[a], J. M. YAÑEZ-LIMÓN[a,*]

[a]*Center for Research and Advanced Studies of IPN, Campus Querétaro, Mexico*
[b]*National Evangelical University, Paseo de los Periodistas #54, Ensanche Miraflores, Santo Domingo, Distrito Nacional, República Dominicana*

Received: November 20, 2019; Revised: February 12, 2020; Accepted: March 8, 2020

Abstract: Pure $K_{0.5}Na_{0.5}NbO_3$ (KNN) and KNN doped with Li^+ (6% mole), La^{3+} (1.66%, 5%, 6% mole), and Ti^{4+} (10% mole) were prepared by mixture of oxides using high-energy milling and conventional solid-state reaction. The effects of the dopant on the physical properties of pure KNN have been evaluated based on the structural, ferroelectric, pyroelectric, and dielectric measurements. The XRD measurements show that KNN pure sample contains a mixture of monoclinic and orthorhombic crystalline phases, with a slightly higher concentration of monoclinic phase. In contrast, all doped samples show a higher concentration of the orthorhombic phase, as well as the presence of a secondary phase ($K_6Nb_{10.8}O_{30}$), also detected by Raman measurements. The samples with a higher concentration of this secondary phase, also present greater dielectric losses and lower values of remnant polarization. The dielectric measurements allowed us to detect temperatures of structural transitions (orthorhombic–tetragonal, O–T) previous to the ferroelectric–paraelectric transition (tetragonal–cubic, T–C), and also in this set of samples, a direct correlation was found between the values of remnant polarization and the corresponding pyroelectric signal response.

Keywords: $K_{0.5}Na_{0.5}NbO_3$ (KNN); lead-free; solid-state reaction; structural properties; pyroelectric properties; dielectric properties; Li, La, Ti doping elements

1 Introduction

Lead-free ceramic systems such as BNT, BT, BCZT, and KNN have become attractive materials for a wide range of applications in the area of electroceramics [1–3], due to their excellent ferroelectric, piezoelectric, and pyroelectric properties that characterize them. Additionally, lead-free materials are friendly to the environment and of low toxicity to human beings [4–8]. Among these systems, KNN has gained attention since Saito *et al.* [9] reported a piezoelectric value of more than 416 pC/N. KNN has an ABO_3 perovskite-type structure and consists of a mixture of solid solutions of $KNbO_3$ and $NaNbO_3$, which exhibits dual, ferroelectric and antiferroelectric behavior, respectively [10,11].

Furthermore, unlike PZT which has a morphotropic phase limit (MPB), KNN shows a polymorphic phase transition (PPT) region, which depends on the composition and temperature [12,13]. When the Na/K

* Corresponding author.
E-mail: jmyanez@cinvestav.mx

ratio is 50/50 [14], the KNN shows excellent ferroelectric, piezoelectric [15], pyroelectric [16], and dielectric properties [17–19] besides having a high ferroelectric–paraelectric transition temperature close to 420 ℃, which allows its practical use in a wide range of temperature. The literature shows several studies related to doping of KNN with atoms of Li, Ta, Sr, Ti, etc. [12,20,21] to improve the physical properties of KNN, thus obtaining similar or even superior values to those reported for PZT.

From the results obtained by Fuentes *et al.* [22], it is interesting to analyze for this system the effects produced by changing the milling method and Li^+ addition. The purpose of this work is to study the physical properties of pure KNN and KNN doped with Li^+ (6% mole), La^{3+} (1.66%, 5%, 6% mole), and Ti^{4+} (10% mole). All materials were synthesized by a combined method of high-energy milling and conventional method of reaction in solid state, using different temperatures of sintering (Table 1). The influence that these dopants cause in the structural, electrical, dielectric, and pyroelectric properties of KNN is analyzed.

2 Experimental

Stoichiometric ceramic samples of pure $K_{0.5}Na_{0.5}NbO_3$ (KNN) and KNN doped with Li^+, La^{3+}, and Ti^{4+} were prepared in the following nominal compositions: $(K_{0.5}Na_{0.5})_{0.94}Li_{0.06}NbO_3$ (KNNLi6), $(K_{0.5}Na_{0.5})_{0.95}La_{0.0166}NbO_3$ (KNNLa1.66), $[(K_{0.5}Na_{0.5})_{0.94}Li_{0.06}]_{0.97}La_{0.01}NbO_3$ (KNNLi6La1), $(K_{0.5}Na_{0.5})_{0.9502}La_{0.0166}Nb_{0.992}Ti_{0.01}O_3$ (KNNLa1.66Ti1), and $(K_{0.5}Na_{0.5})_{0.85}La_{0.05}Nb_{0.992}Ti_{0.01}O_3$ (KNNLa5Ti1), using high-energy mechanical milling for mixing starting reagents and conventional synthesis by solid-state reaction. The precursor materials used were powders of K_2CO_3 (99%, MEYER), Na_2CO_3 (99.5%, JT Baker), Nb_2O_5 (99.99%, SIGMA-ALDRICH), Li_2CO_3 (99%, SIGMA-ALDRICH), La_2O_3 (99.9%, SIGMA-ALDRICH), and TiO_2 (99% SIGMA-ALDRICH). The powders were processed in a high-energy mill Spex 8000 for 90 min, using zirconium balls of 10.24 and 4.8 mm in diameter with a 10:1 ratio in weight (powders:balls) using nylamid vials. The resultant mixture of powders after milling was calcined at 800 ℃ for 3 h in the form of 12.7 mm diameter pellets. Subsequently, the samples were again grounded for 15 min and sieved with a 44 μm mesh. The resulting powders were pressed uniaxially at a pressure of 63 MPa to obtain cylindrical pellets of 12.7 mm in diameter, adding polyvinyl alcohol in 5% by weight of the sample as a binder. Finally, the samples were encapsulated in a platinum crucible and sintered at different temperatures in the range of 1080–1120 ℃ for 2.5 h, according to the data reported in Table 1. The density of the samples was measured by the Archimedes' principle. The relative density was calculated taking into account the theoretical densities of orthorhombic, monoclinic, and secondary phases according to the phase concentration estimated by XRD analysis in each sample as displayed in Table 2.

The crystal structure of the samples was determined using X-ray diffraction (XRD) using a Rigaku Dmax-2100 diffractometer with copper radiation (λ = 1.5418 Å) and a 2θ sweep in a range of 15°–80°. The Raman characterization was done using a Spex 1403 spectrometer, with a resolution of 1 cm^{-1}, in a range of 100–1000 cm^{-1}, using a Lexel 95 argon laser and the excitation line at 488 nm. Microstructure analysis was performed on the fractured surfaces by scanning electron microscopy using a Philips model ESEM XL30 electronic microscope operating at 25 kV and with a current less than 85 μA. For the ferroelectric measurements, silver paint was placed on both surfaces of the samples and subjected to a thermal treatment at 300 ℃ for 30 min. The measurements of the hysteresis loops as a function of the applied electric field (*P–E* curves) were carried out with RADIANT Technologies INC equipment, to which a high-voltage source TReK model 609E-6 of 4000 volts was coupled. To evaluate the behavior of the pyroelectric response, the ceramic samples with silver electrodes were polarized for 30 min at 16 kV/cm. The evaluation of the pyroelectric properties was carried out in a system for measuring photothermal properties, which consists of a 100 mW laser diode as a source of illumination and heating. The

Table 1 Sintering temperatures and relative densities of the ceramic samples. The theoretical density is 4.64, 4.54, and 4.57 g/cm^3 for the monoclinic (JCPDS 77-0038), orthorhombic (JCPDS 00-065-0275), and secondary phase ($K_6Nb_{10.8}O_{30}$, PDF#70-5051), respectively

Sample	Sintering temperature (℃)	Relative density ρ_r (%)
KNN	1100	94.03
KNNLi6	1080	94.77
KNNLa1.66	1120	98.82
KNNLi6La1	1120	98.43
KNNLa1.66Ti1	1100	96.70
KNNLa5Ti1	1100	95.80

Table 2 Crystal lattice parameters of the crystalline structure of the ceramic samples, obtained by the Rietveld analysis

Sample	Crystal phase	Lattice parameters (Å)				Crystal phase (%)	Crystallite size (nm)
		a	*b*	*c*	*β*		
KNN	Monoclinic	7.97	7.86	7.97	90.3	52.39	80.32
	Orthorhombic	3.94	5.63	5.64	—	46.85	76.66
KNNLi6	Monoclinic	7.97	7.88	7.93	90.6	15.15	102.1
	Orthorhombic	3.94	5.67	5.66	—	71.75	69.7
	$K_6Nb_{10.8}O_{30}$	12.58	—	3.95	—	13.09	43.21
KNNLi6La1	Monoclinic	7.93	7.90	7.96	89.63	15.82	55.92
	Orthorhombic	3.94	5.64	5.66	—	69.81	55.80
	$K_6Nb_{10.8}O_{30}$	12.57	—	3.96	—	14.35	37 .53
KNNLa1.66	Orthorhombic	3.94	5.60	5.61	—	60.75	25.69
	$K_6Nb_{10.8}O_{30}$	12.56	—	3.92	—	39.24	26.15
KNNLa1.66Ti1	Orthorhombic	3.97	5.62	5.61	—	89.26	30.25
	$K_6Nb_{10.8}O_{30}$	12.53	—	3.96	—	10.73	101.9
KNNLa5Ti1	Orthorhombic	3.94	5.61	5.63	—	84.34	31.42
	$K_6Nb_{10.8}O_{30}$	12.57	—	3.93	—	15.65	48.11

radiation in the sample is modulated after going through a Stanford Research system model SR540 mechanical chopper. The sample acts as a pyroelectric sensor, and the periodic incidence of the laser produces periodic heating of the sample that, in turn, produces an AC voltage on the opposite sides of the sample, which is recorded in amplitude and phase by an EG&G Princetown Applied Research lock-in amplifier. The AC voltage, the pyroelectric coefficient, and the average temperature of the sample are related by the following equation [23,24]:

$$V(\omega)=\frac{pl_{\mathrm{p}}T_{\mathrm{p}}(\omega)}{k\varepsilon_0}\exp(\omega t) \tag{1}$$

where ω is the frequency of the modulated light, p is the pyroelectric coefficient, l_{p} and T_{p} are the thickness and average temperature of the pyroelectric sample respectively, and k and ε_0 are the dielectric constant and the vacuum permittivity respectively. Maintaining the power of the incident laser constant in samples with a constant thickness, the pyroelectric signal obtained in the same frequency range allows us to estimate comparatively the behavior of the pyroelectric coefficient, which is related with the variation with temperature of the spontaneous polarization of the sample $p=\left(\partial P_{\mathrm{s}}/\partial T\right)_{E,X}$ maintaining the electric field (E) and stress (X) constant [25].

The dielectric characterization was made by a Keysight E4990A impedance analyzer with a measurement range of 20 Hz–10 MHz, coupled with a system of data acquisition and temperature control in a cylindrical furnace built in our laboratory. This allows measurements of impedance and capacitance as a function of temperature in a range from room temperature to 500 ℃ at different frequencies.

3 Results and discussions

3.1 Microstructure characterization

Sintering temperature and relative density of the studied samples are shown in Table 1. The XRD patterns for all sintered samples are shown in Fig. 1. Comparatively, it can be seen that the peaks of KNN correspond mostly to the monoclinic phase, whereas in the KNNLi6, KNNLi6La1, KNNLa1.66, KNNLa5Ti1, and KNNLa1.66Ti1 samples, the majority phase is orthorhombic. The two peaks located around 46° for the samples KNNLi6 and KNNLi6La1 belong to a combination of monoclinic and orthorhombic phases. These peaks belong to the planes (400) for the monoclinic phase and (022) and (200) for the orthorhombic one [22,26,27]. Two reflections are observed in KNN (monoclinic + orthorhombic) but only one reflection is observed for the orthorhombic phase. It can be seen that this reflection of the doped samples undergoes a shift as a result of the substitution of the atoms in the original cell, which suggests a contraction of the unit cell. The formation of the secondary phase is attributed to the substitution of the La^{3+} and Li^{+} dopant at the site occupied by Na^{+} and K^{+}. This effect might promote the volatilization of Na^{+} more than K^{+} [28,29], resulting in a phase rich in K^{+}, as can be seen in Fig. 1. The peaks marked with "*" correspond to a secondary tetragonal

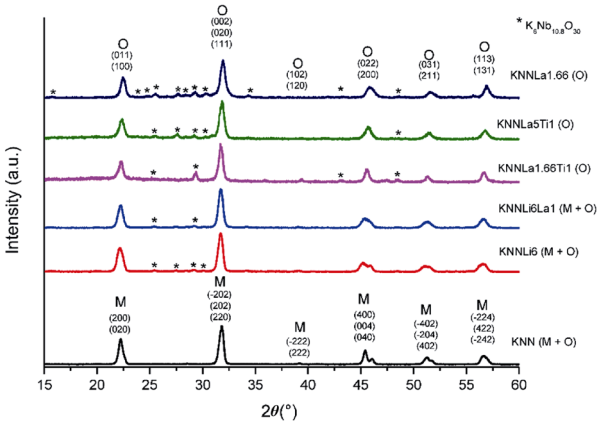

Fig. 1 Diffraction patterns of ceramic samples. M and O stand for the monoclinic and the orthorhombic phases, respectively.

phase identified as potassium, niobium ($K_6Nb_{10.8}O_{30}$) [28]. The non-doped KNN sample does not present the secondary tetragonal phase $K_6Nb_{10.8}O_{30}$.

The crystal lattice parameters were determined by performing a Rietveld refinement to the X-ray diffraction patterns using the MAUD (Materials Analysis Using Diffraction) program [30], where the CIF files for $K_{0.65}Na_{0.35}NbO_3$, $K_{0.507}Na_{0.537}NbO_3$, and $K_6Nb_{10.8}O_{30}$ of the monoclinic, orthorhombic, and secondary phase structures were used (JCPDS 70-0038, JCPDS 00-065-0275, JCPDS 70-5051) respectively. Figure 2 is an example of how the Rietveld refinement was made for the KNN sample. The lattice parameters, percentage of phase concentration, and crystallite size obtained for these phases are shown in Table 2.

The sample of pure KNN has a slightly higher concentration of the monoclinic phase, 52.39% against 46.85% of the orthorhombic phase. Doping shows apparent changes, reversing the concentration of phases,

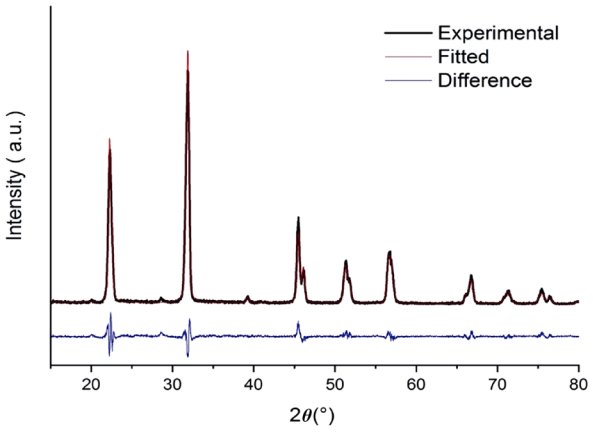

Fig. 2 Rietveld refinement of the XRD pattern of the pure KNN sample.

in addition to the appearance of a secondary phase $K_6Nb_{10.8}O_{30}$; the KNNLa1.66Ti1 sample shows the highest concentration of orthorhombic phase, 89.26% and 10.73% of the secondary phase without the presence of the monoclinic phase. Also, in general, the crystallite size shows a reduction with the doping.

Figure 3(a) shows the typical Raman vibrations corresponding to a perovskite phase [31] for all samples. According to the Ross model [32], the KNN modes are classified in 6 internal modes of the octahedron NbO_6, of which, $A_{1g}(\nu_1)$, $E_g(\nu_2)$, and $T_{1u}(\nu_3)$ are associated with stretching vibrations, and $T_{1u}(\nu_4)$, T_{2g} (ν_5), and $F_{2u}(\nu_6)$ are bending modes [33]. The internal modes $\nu_1(A_{1g})$, $\nu_2(E_g)$, $\nu_4(T_{1u})$, $\nu_5(T_{2g})$, $\nu_6(T_{2u})$, and $\nu_1(A_{1g})+\nu_5(T_{2g})$ of the octahedron NbO_6 appear in the range of 194–871 cm^{-1}.

Comparatively, most of the doped samples exhibit 7 characteristic modes associated with the orthorhombic phase [33–35], according to XRD results. Moreover, 10 Raman bands were observed in spectra of the KNN sample (Fig. 3) which is similar to the Raman spectra reported, corresponding to the monoclinic phase [36].

The Raman spectra of the doped samples (higher orthorhombic phase concentration) underwent important shifts (Fig. 3(b)) that differ in frequency value concerning the KNN spectrum (monoclinic phase) by dopant effect.

Figure 3(b) shows the present modes, at the frequency range of 150–500 cm^{-1} and 520–700 cm^{-1} obtained by the deconvolution of the experimental spectra. The band located at 141 cm^{-1} for KNN (Fig. 3(a)) is attributed to mixed modes [36]. On the other hand, the same band is shifted to 152 cm^{-1} for KNNLi6 due to the substitution of Li^+ into Na^+/K^+ sites. KNNLi6

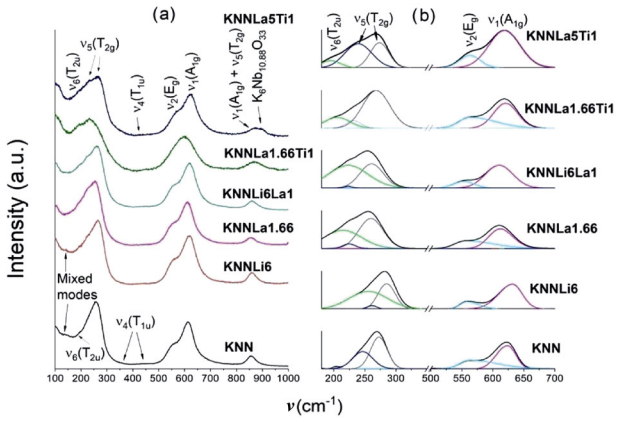

Fig. 3 Raman spectra at room temperature of pure and doped KNN: (a) at the frequency range of 100–1000 cm^{-1}; (b) the deconvolution bands centered at approximately 260 cm^{-1} (ν_5 and ν_6) and 630 cm^{-1} (ν_2 and ν_1).

undergoes a shift at high frequencies (Fig. 3(b)) since the Li^+, which is an atom that replaces the atoms of Na^+ and K^+ at site A, is a lighter atom than those it replaces. Likewise, the constant force is increased and can be related to an increase of the structural disorder due to the substitution of Na/K atoms by Li [36], while the samples doped with La^{3+} and Ti^{4+} which are heavier atoms substitute the Na^+ and K^+ atoms at site A and Nb^{5+} at site B, respectively. This shows a shift towards lower frequencies of most of the modes (Fig. 3(b)) and the force constants decrease.

The $\nu_5(T_{2g})$ and $\nu_1(A_{1g})$ modes are very intense bands in the samples due to the high symmetry of the octahedron, which is affected when doping with different ions (Fig. 3(a)). In the spectral range of 180–350 cm^{-1}, three Raman modes are detected for all samples (both monoclinic and orthorhombic phases). The modes with a range of 360–510 cm^{-1} (Fig. 4(a)), two bands are shown for KNN (ν_4 modes) [36] and only one Raman band (ν_4) is shown for the other samples. In modes that range from 500 to 700 cm^{-1}, the characteristic bands (ν_2 and ν_1) for doped KNN and pure KNN are shown.

The $\nu_1+\nu_5$ Raman mode (Fig. 4(b)), which is present in the doped samples, is characteristic for both the monoclinic and orthorhombic phases, and it is sensitive to the concentration of Na^+ and K^+ [37]. Additionally, the $\nu_1+\nu_5$ mode is well defined for KNN, but for the doped KNN, the $\nu_1+\nu_5$ mode is broad and is more noticeable for samples containing La^{3+} and Ti^{4+}.

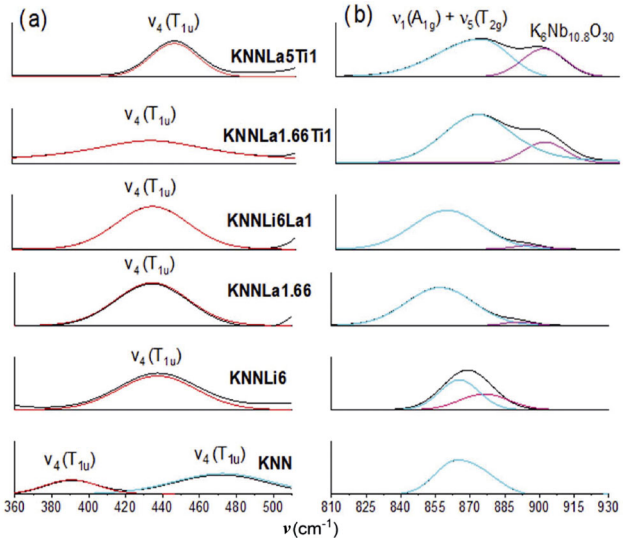

Fig. 4 Deconvoluted detail of (a) modes ν_4 at frequencies ranging from 360 to 510 cm^{-1} and (b) $\nu_1+\nu_5$ and $K_6Nb_{10.8}O_{30}$ at the frequencies ranging from 810 to 930 cm^{-1}.

The doped samples show an additional vibrational mode (Fig. 4(b)) detected at 876 cm^{-1} for KNNLi6, 891 cm^{-1} for KNNLa1.66, 898 cm^{-1} for KNNLa1.66Ti1, 897 cm^{-1} for KNNLa5Ti1, and 891 cm^{-1} for KNNLa6Li1. This is associated with the formation of the secondary phase $K_6Nb_{10.8}O_{30}$, also identified by XRD. The presence of this kind of secondary phase has been previously reported by other authors [28].

In the scanning electron microscopy (SEM) analysis, the images of the sintered ceramic samples are shown (Fig. 5). Here, a dependence of the grain size with the doping, observing a decrease of the grain size in all doped samples can be observed.

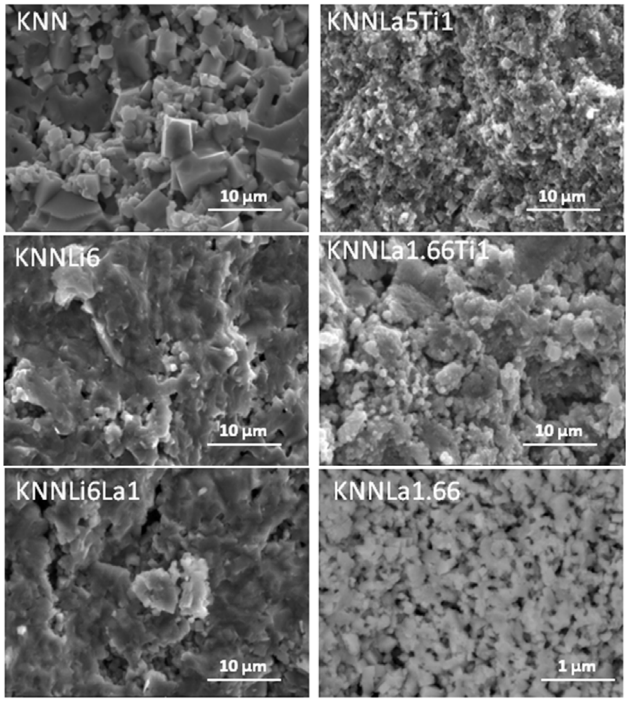

Fig. 5 SEM images of pure and doped KNN sintered at different temperatures.

All micrographs show the typical morphology of ceramics based on alkaline niobates. The grain size measurements demonstrated that pure KNN shows the largest grain size (1.16 μm) and it decreases with the addition of dopants. The large error bar, shown in the KNN sample, is because there are two ranges of grain size distributions related to the monoclinic and orthorhombic phases, corresponding to the results obtained in XRD (Table 2), where the monoclinic and orthorhombic phases are in similar proportions [32,33]. The sample that showed the smallest grain size is KNNLa1.66 (Fig. 6) with an average grain size of 0.4 μm. Previous studies report that the effect of doping promotes the diffusion of substituted ions to the grain

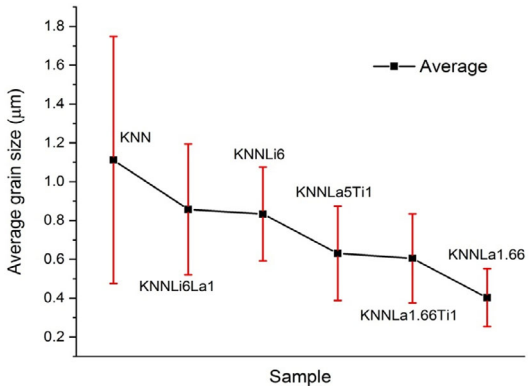

Fig. 6 Decrease in average grain size in ceramic samples by the action of dopants.

boundaries and contributes to the decrease in grain size, as observed in this case. Therefore, the addition of dopants inhibits the grain growth in all doped samples [38], and promotes a higher concentration of the orthorhombic phase according to XRD results.

3. 2 Ferroelectric characterization

Figure 7 shows the hysteresis loop of the different samples characterized at room temperature with an applied electric field of up to 60 kV/cm in a period of 10 ms. The maximum polarization obtained (Table 3) is achieved for the KNNLa1.66Ti1 sample. The polarization drop near the maximum polarization field is observed in KNN, KNNLi6, and KNNLa1.66Ti1, accompanied by a discontinuity in the polarization for $E = 0$. This effect is attributed to conductivity losses caused by vacancies in the crystal lattice and impurities such as the secondary phase seen previously in XRD. The samples of KNNLi6La1, KNNLa1.66, and KNNLa5Ti1 present a typical ferroelectric curve with no polarization drop to the applied maximum field, as shown in Fig. 7. The remnant polarization of the samples exhibits a decreasing tendency as a function of the increase in the quantity of secondary phase ($K_6Nb_{10.8}O_{30}$), as displayed in Fig. 8. Here, higher amounts of secondary phase that tend to reduce the remnant polarization [28] are observed, and therefore, the applied voltage is not used efficiently. It is also observed in Fig. 7 that the samples with the lowest coercive field are those of pure KNN and KNNLa5Ti1 with 11.52 and 10.43 kV/cm, respectively. The coercive field depends on the relaxation that occurs during the inversion of the polarization that causes the displacement of the domain boundary, as well as the inversion of the polarization in the direction of the applied field, depending on the structure as well as the grain and domain size [39].

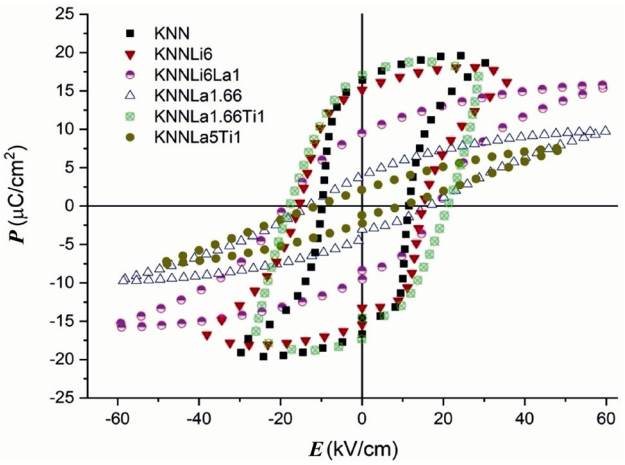

Fig. 7 Cycles of ferroelectric hysteresis of ceramic samples.

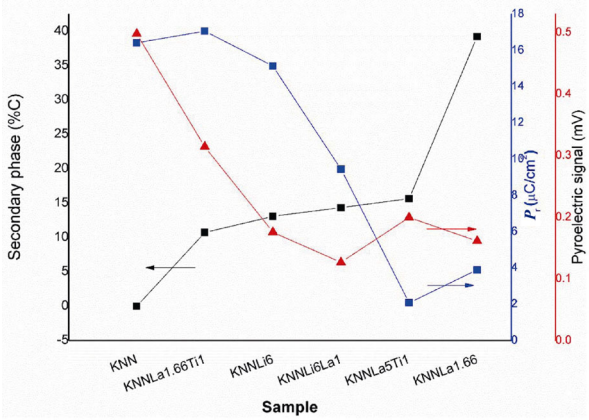

Fig. 8 Comparison of the amount of secondary phase ($K_6Nb_{10.8}O_{30}$), the remnant polarization, and pyroelectric signal of the ceramic samples.

Table 3 Remnant polarization and the coercive electric field of the analyzed samples

Sample	P_r (μC/cm^2)	E_c (kV/cm)
KNNLa1.66Ti1	17.06	21.16
KNN	16.42	11.52
KNNLi6	15.14	14.98
KNNLi6La1	9.45	18.72
KNNLa1.66	3.90	16.73
KNNLa5Ti1	2.09	10.43

3. 3 Pyroelectric response

Figure 9 shows the results of the pyroelectric response (AC amplitude in volt) as a function of the modulation frequency for the set of samples. The general behavior of the pyroelectric signal is an exponential decay (Eq. (1)) [23,24]. The voltage amplitude of the signal depends on the frequency and is proportional to the

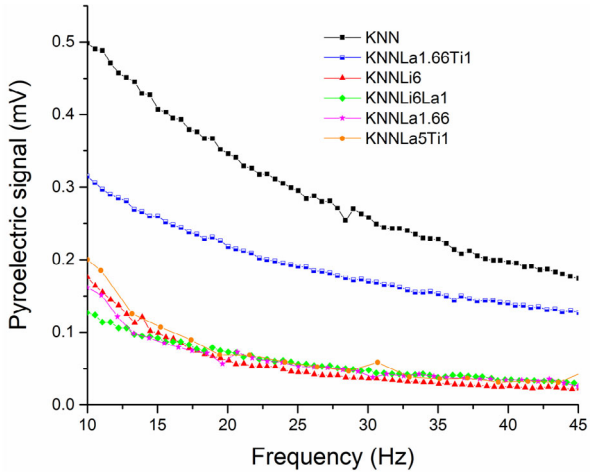

Fig. 9 Pyroelectric response of ceramic samples. All samples were polarized under the application of an electric field of 16.6 kV/cm for 30 min.

pyroelectric coefficient which depends on the variation with the temperature of the remnant polarization of the samples. The largest values of the signal were obtained for the samples of pure KNN (0.5 mV) and KNNLa1.66Ti1 (0.31 mV), both at 10 Hz. In Fig. 8, a comparison between the pyroelectric signal and the P_r is made and it is observed that, for those samples with lower values of P_r, the corresponding values of the pyroelectric signal also tend to decrease.

3. 4 Dielectric characterization

The dielectric behavior of materials with temperature, particularly ferroelectric, is to increase its value to a maximum that corresponds to the transition from ferroelectric to paraelectric phase. These contributions to the permittivity are given by different contributions of the different polarization types that occur during the measurement itself, as well as the contributions of the different frontiers presented in the material (crystallite, domain, grain border, and interphase between the sample and electric contact). Some authors suggest that, in this case, the increases of dielectric permittivity with temperature are due to the contribution of the polarization of space charges [40]. As a result of introducing dopants, vacancies are created (crystalline imperfections) and this changes the contribution of the polarization of space charges. The relative dielectric permittivity of a material is affected by dipolar, electronic, ionic, and interfacial polarization [40].

According to Saito *et al.* [9], in the KNN (in a range of 25–500 ℃) system, a first peak presented in the curve of ε vs. T around 220 ℃ corresponds to the orthorhombic–tetragonal phase transition. Likewise, a second peak, of greater permittivity value, corresponds to the ferroelectric–paraelectric transition, where the material passes from tetragonal to cubic phase (also known as Curie temperature). Some authors suggest that the predominant polarization mechanism changes from dipolar to interfacial, which is reflected in a rise of the relative dielectric permittivity in the ferroelectric–paraelectric transition [40].

Different authors have reported that, in KNN, the effect of Li increases the tetragonal–cubic phase transition temperature ($T_{T–C}$) and decreases the orthorhombic–tetragonal phase transition temperature [41]. It also decreases the remnant polarization, the coercive field, and the mechanical quality factor (Q_m) [42]. On the other hand, the La^{3+} causes an increase in the temperature of orthorhombic–tetragonal transition $T_{O–T}$ and a decrease of the T_C [43]. The low-temperature ferroelectric–ferroelectric transition (O–T) is dominated by a dipolar polarization mechanism and this can be modified by the effect of dopant, which can increase or decrease the influence of this mechanism in magnitude and temperature.

In Fig. 10 it is appreciated that pure KNN shows an O–T transition at 207 ℃ followed by a T–C transition (ferroelectric–paraelectric) at 402 ℃, close with what is reported in the literature [41]. The effect of the different dopants is confirmed: the Li increases the cubic–tetragonal phase transition temperature ($T_{T–C}$) but only when combined with La, something not reported in the literature. This raises T_C to 445 ℃, if it coincides with the decrease in the O–T temperature, the one that occurs at 160 ℃ (Fig. 11). The results obtained for KNNLi6 do not coincide exactly since both transition temperatures decrease, although the O–T decreases around 100 ℃ concerning pure KNN and the T–C transition occurs only 20 ℃ below the KNN without doping. The effect of lanthanum depends on the concentration and whether a substitution occurs at position B of the perovskite structure since it goes to site A, where the K^+ and Na^+ are located. These changes occur because lanthanum entering in the structure weakens long-range interaction, allowing changes to occur at lower temperatures (mainly T_C). In the interactions where the atoms of Li^+, Na^+, and K^+ are present, the participating orbitals are the "s" orbitals, which are very strong and are stronger for the Li^+, which is why the Curie temperature increases. However, the orbitals that participate in the case of La^{3+} are hybrid "sd" orbitals ($6s^2$–$5d^1$), which are less strong than "s",

so the T_C temperature decreases.

When Ti^{4+} is introduced at site B (sample KNNLa5Ti1), again the participating orbitals are hybrid "sd" orbitals ($4s^2$–$3d^2$). In addition to lowering the Curie temperature. The O–T transition appears around 234 ℃ (Fig. 11); however, for KNNLa1.66Ti1 it was only possible to identify the Curie transition (T_C). In addition to the effect that dopant causes in the transition temperatures, there is a noticeable decrease in the magnitude of the relative dielectric permittivity (Fig. 10). It is important to point out the decrease in the relative dielectric permittivity, in particular between 25 and 100 ℃, as it appears in detail in Fig. 10, varying from 937.6 for KNN to 205.9 for KNNLi6.

The permittivity profile for the KNNLa1.66Ti1 and KNNLa5Ti1 samples corresponds to a diffuse phase transition, due to the simultaneous effect of the replacement of the La^{3+} ion and Ti^{4+} at sites A and B, respectively [44].

The dielectric losses are high but show the inhomogeneity of the samples due to the presence of three phases (monoclinic, orthorhombic, and $K_6Nb_{10.8}O_{30}$) at room temperature. All values of relative dielectric permittivity at room temperature and transition temperatures for 1 kHz are also shown in Table 4.

For applications where the capacity is used in the temperature range of 25–100 ℃ the characteristics of the selected material must be constant or with a linear behavior, the candidates being KNN, KNNLa1.66Ti1, and KNNLa5Ti1 samples.

The results obtained in this study concerning to those reported in previous works [12,20,21] with dopants in a similar concentration range, show some coincidences and also important differences. The effect of dopants, in general, is to induce a decrease in grain size, as well as a decrease in the remnant polarization if compared with pure KNN. Furthermore, a decrease in T–C and O–T transition temperatures is also observed with the increase in dopant concentration. However, in our case, the samples KNNLi6La1 and KNNLa5Ti1 show an increase in their transition temperatures for T–C and O–T, respectively.

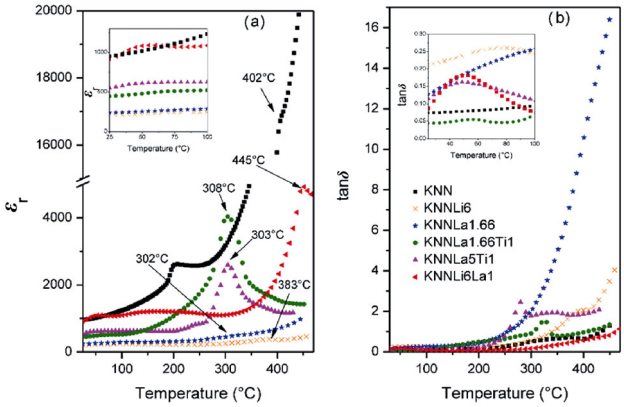

Fig. 10 (a) Relative dielectric permittivity (ε_r) and (b) dielectric loss (tanδ) of ceramic samples as a function of temperature at 1 kHz. Both cases show details of behaviors at low temperature.

Table 4 Dielectric permittivity at room temperature and transition temperatures for orthorhombic–tetragonal (O–T) and tetragonal–cubic (T–C) or Curie temperature transition (T_C)

Sample	ε_r (room temperature)	Transition temperature (℃)	
		O–T	T–C = T_C
KNN	937.6	207	402
KNNLi6	205.9	82	383
KNNLi6La1	967.4	160	445
KNNLa1.66	235.2	122	302
KNNLa1.66Ti1	439.6	—	308
KNNLa5Ti1	531.6	234	303

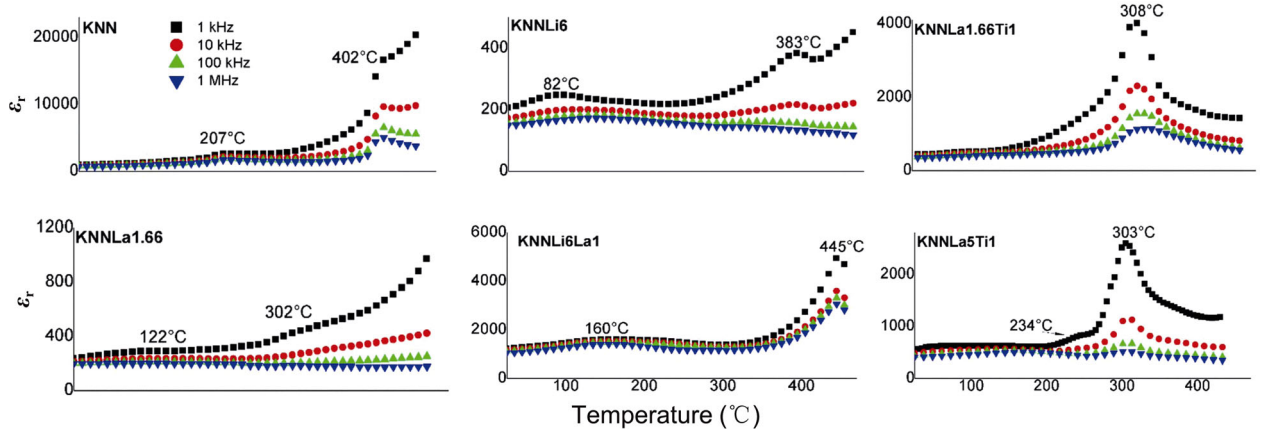

Fig. 11 Dependence of dielectric function with the temperature at frequencies of 1, 10, 100 kHz and 1 MHz.

In these previous works, the authors report mixtures of orthorhombic and tetragonal phases in their samples; however, in our study, due to the processing conditions, milling method, precursors, and doping elements used, we find a mixture of monoclinic and orthorhombic phases. Additionally, the concentration range of dopants used in this work generates the formation of low amounts of the secondary phase $K_6Nb_{10.8}O_{30}$. Finally, the values obtained from the dielectric permittivity at room temperature are similar in the temperature range of 500 and 1000 ℃.

4 Conclusions

We have studied the effect of Li^+, La^{3+}, and Ti^{4+} dopants on the structural, morphological, ferroelectric, and dielectric properties of KNN. The densities of all doped samples showed higher density values than pure KNN. From XRD analyses, it was confirmed that the pure KNN sample presents a mixture of monoclinic and orthorhombic crystalline phases. In contrast, the addition of La^{3+}, Ti^{4+}, and Li^+ induces an increase in the concentration of the orthorhombic phase and also a secondary tetragonal phase of $K_6N_{10.8}O_{30}$. The Raman results confirmed the presence of the monoclinic (KNN) and orthorhombic (doped KNN) phases in good agreement with the XRD results and a secondary phase $K_6Nb_{10.8}O_{30}$. Moreover, it was observed that there is a reduction in grain size due to doping, in which KNN showed the highest average grain size. The study of the ferroelectric properties showed a maximum value of polarization remaining for the composition of KNNLa1.66Ti1 followed by KNN. It was observed that there is a direct dependence between the amount of secondary phase present and the reduction of the remnant polarization. The pyroelectric response resulted in a maximum voltage signal for un-doped KNN and shows the same trend as the remnant polarization of the samples. The relative permittivity and Curie temperature showed maximum values in the KNNLi6La1 sample, as well as a decrease in the O–T transition temperature of the doped samples. At room temperature, sample KNNLa1.66Ti1 showed the lowest dielectric losses. For our samples, those that have a greater remnant polarization (P_r) also have a higher pyroelectric response. The results obtained are strongly determined by the milling process used.

Acknowledgements

The authors express their thanks to CONACYT for funding this research through projects CB-240460 and LN-295261, and to LIDTRA for the facilities in the use of experimental infrastructure. To the research assistants Martín Adelaido Hernández Landaverde, Rivelino Flores Farias, Agustín Galindo Sifuentes, and Carlos Alberto Avila Herrera. C. Montero-Tavera and F. D. Cortes-Vega thank CONACYT for the scholarships granted to complete the Ph.D. studies and postdoctoral position, respectively.

References

[1] Ioachim A, Toacsan MI, Banciu MG, *et al*. BNT ceramics synthesis and characterization. *Mat Sci Eng B* 2004, **109**: 183–187.

[2] Sonia, Patel RK, Prakash C, *et al*. Characterizations of BT ceramics synthesized by modified solid state route. *AIP Conf Proc* 2011, **1372**: 116–120.

[3] Frattini A, di Loreto A, de Sanctis O, *et al*. BCZT ceramics prepared from activated powders. *Procedia Mater Sci* 2012, **1**: 359–365.

[4] Sanín LH, González-Cossío T, Romieu I, *et al*. Acumulación de plomo en hueso y sus efectos en la salud. *Salud Pública Méx* 1998, **40**: 359–368.

[5] Rödel J, Webber KG, Dittmer R, *et al*. Transferring lead-free piezoelectric ceramics into application. *J Eur Ceram Soc* 2015, **35**: 1659–1681.

[6] Goyer RA. Lead toxicity: Current concerns. *Environ Health Perspect* 1993, **100**: 177–187.

[7] Lockitch G. Perspectives on lead toxicity. *Clin Biochem* 1993, **26**: 371–381.

[8] Patrick L. Lead toxicity, a review of the literature. Part I: Exposure, evaluation, and treatment. *Altern Med Rev* 2006, **11**: 2–22.

[9] Saito Y, Takao H, Tani T, *et al*. Lead-free piezoceramics. *Nature* 2004, **432**: 84–87.

[10] Baier-Saip JA, Ramos-Moor E, Cabrera AL. Raman study of phase transitions in $KNbO_3$. *Solid State Commun* 2005, **135**: 367–372.

[11] Chang YF, Yang ZP, Dong MY, *et al*. Phase structure, morphology, and Raman characteristics of $NaNbO_3$ particles synthesized by different methods. *Mater Res Bull* 2009, **44**: 538–542.

[12] Dai YJ, Zhang XW, Zhou GY. Phase transitional behavior in $K_{0.5}Na_{0.5}NbO_3$–$LiTaO_3$ ceramics. *Appl Phys Lett* 2007, **90**: 262903.

[13] Wang J, Luo LH. Probing the diffusion behavior of polymorphic phase transition in $K_{0.5}Na_{0.5}NbO_3$ ferroelectric ceramics by Eu^{3+} photoluminescence. *J Appl Phys* 2018, **123**: 144102.

[14] Kumar P, Pattanaik M, Sonia. Synthesis and characterizations of KNN ferroelectric ceramics near 50/50 MPB. *Ceram Int* 2013, **39**: 65–69.

[15] Guo YP, Kakimoto KI, Ohsato H. Phase transitional behavior and piezoelectric properties of $(Na_{0.5}K_{0.5})NbO_3$–$LiNbO_3$ ceramics. *Appl Phys Lett* 2004, **85**: 4121–4123.
[16] Lau ST, Cheng CH, Choy SH, *et al*. Lead-free ceramics for pyroelectric applications. *J Appl Phys* 2008, **103**: 104105.
[17] Wattanawikkam C, Chootin S, Bongkarn T. Crystal structure, microstructure, dielectric and piezoelectric properties of lead-free KNN ceramics fabricated via combustion method. *Ferroelectrics* 2014, **473**: 24–33.
[18] Singh R, Kulkarni AR, Harendranath CS. Dielectric and piezoelectric properties of KNN synthesized using colloidal coating approach. *AIP Conf Proc* 2013, **1512**: 514–515.
[19] Sharma S, Kumari S, Rai R, *et al*. Effect of Na on the structural and electrical properties of lead-free sodium potassium niobate ceramics. *Integr Ferroelectr* 2016, **168**: 115–129.
[20] Lin DM, Kwok KW, Chan HLW. Phase transition and electrical properties of $(K_{0.5}Na_{0.5})(Nb_{1-x}Ta_x)O_3$ lead-free piezoelectric ceramics. *Appl Phys A* 2008, **91**: 167–171.
[21] Park HY, Cho KH, Paik DS, *et al*. Microstructure and piezoelectric properties of lead-free $(1–x)(Na_{0.5}K_{0.5})NbO_3$–$xCaTiO_3$ ceramics. *J Appl Phys* 2007, **102**: 124101.
[22] Fuentes J, Portelles J, Pérez A, *et al*. Structural and dielectric properties of La- and Ti-modified $K_{0.5}Na_{0.5}NbO_3$ ceramics. *Appl Phys A* 2012, **107**: 733–738.
[23] Mandelis A, Zver MM. Theory of photopyroelectric spectroscopy of solids. *J Appl Phys* 1985, **57**: 4421–4430.
[24] Rivera-Ruedas MG, Flores-Noria JR, García-Rodríguez FJ, *et al.* PZT ferroelectric ceramics obtained by sol–gel method using 2-metoxyethanol route for pyroelectric sensors. *Mater Res Innov* 2009, **13**: 375–378.
[25] Batra AK, Aggarwal MD. *Pyroelectric Materials: Infrared Detectors, Particle Accelerators, and Energy Harvesters*. SPIE Press, 2013.
[26] Durruthy-Rodríguez MD, Hernández-García M, Portelles J, *et al*. Strong emissions of blue–yellow–red regions of La and Ti modified $KNaNbO_3$ ferroelectric ceramics. *J Adv Ceram* 2015, **4**: 183–189.
[27] Zhen YH, Li JF. Normal sintering of $(K,Na)NbO_3$-based ceramics: Influence of sintering temperature on densification, microstructure, and electrical properties. *J Am Ceram Soc* 2006, **89**: 3669–3675.
[28] Vendrell X, García JE, Cerdeiras E, *et al*. Effect of lanthanide doping on structural, microstructural and functional properties of $K_{0.5}Na_{0.5}NbO_3$ lead-free piezoceramics. *Ceram Int* 2016, **42**: 17530–17538.
[29] Shannon RD. Revised effective ionic radii and systematic studies of interatomic distances in halides and chalcogenides. *Acta Cryst* 1976, **A32**: 751–767.
[30] Ferrari M, Lutterotti L. Method for the simultaneous determination of anisotropic residual stresses and texture by X-ray diffraction. *J Appl Phys* 1994, **76**: 7246–7255.
[31] Kakimoto KI, Akao K, Guo YP, *et al*. Raman scattering study of piezoelectric $(Na_{0.5}K_{0.5})NbO_3$–$LiNbO_3$ ceramics. *Jpn J Appl Phys* 2005, **44**: 7064–7067.
[32] Ross SD. The vibrational spectra of lithium niobate, barium sodium niobate and barium sodium tantalate. *J Phys C: Solid State Phys* 1970, **3**: 1785–1790.
[33] Shiratori Y, Magrez A, Pithan C. Phase transformation of $KNaNb_2O_6$ induced by size effect. *Chem Phys Lett* 2004, **391**: 288–292.
[34] Vendrell X, García JE, Bril X, *et al*. Improving the functional properties of $(K_{0.5}Na_{0.5})NbO_3$ piezoceramics by acceptor doping. *J Eur Ceram Soc* 2015, **35**: 125–130.
[35] Wang Z, Gu HS, Hu YM, *et al*. Synthesis, growth mechanism and optical properties of $(K,Na)NbO_3$ nanostructures. *CrystEngComm* 2010, **12**: 3157–3162.
[36] Trodahl HJ, Klein N, Damjanovic D, *et al*. Raman spectroscopy of $(K,Na)NbO_3$ and $(K,Na)_{1-x}Li_xNbO_3$. *Appl Phys Lett* 2008, **93**: 262901.
[37] Vendrell X, Raymond O, Ochoa DA, *et al*. Growth and physical properties of highly oriented La-doped $(K,Na)NbO_3$ ferroelectric thin films. *Thin Solid Films* 2015, **577**: 35–41.
[38] Durruthy-Rodríguez MD, Pérez-Fernández LD, Peláiz-Barranco A, *et al*. Structural and dielectric characteristics of donor dopants in A and B places of perovskite ceramic PZT 54/46. *Appl Phys A* 2009, **95**: 423–428.
[39] Chen IW. Dielectric and ferroelectric ceramics: Interfaces. In *Encyclopedia of Materials: Science and Technology*. Elsevier, 2001: 2152–2157.
[40] Singh AK, Goel TC, Mendiratta RG, *et al*. Magnetic properties of Mn-substituted Ni–Zn ferrites. *J Appl Phys* 2002, **92**: 3872–3876.
[41] Du HL, Tang FS, Liu DJ, *et al*. The microstructure and ferroelectric properties of $(K_{0.5}Na_{0.5})NbO_3$–$LiNbO_3$ lead-free piezoelectric ceramics. *Mat Sci Eng B* 2007, **136**: 165–169.
[42] Lin DM, Kwok KW, Chan HLW. Microstructure, phase transition, and electrical properties of $(K_{0.5}Na_{0.5})_{1-x}Li_x(Nb_{1-y}Ta_y)O_3$ lead-free piezoelectric ceramics. *J Appl Phys* 2007, **102**: 034102.
[43] Durruthy-Rodríguez MD, Gervacio-Arciniega JJ, Portelles J, *et al*. PFM characterization of $(K_{0.5}Na_{0.5})_{0.95}La_{0.05}(Nb_{0.9}Ti_{0.05})O_{2.9}$ ceramics lead free. *Appl Phys A* 2013, **113**: 515–519.
[44] Mahesh P, Pamu D. Raman and dielectric studies on lead free $(K_{0.5}Na_{0.5})NbO_3$ piezoelectric ceramics. *IOP Conf Ser: Mater Sci Eng* 2015, **73**: 012141.